Smectic Liquid Crystal Fibres as Light-guides

Oliver Liebe

A thesis presented for the degree of
Bachelor of Physics, B.Sc.

Department of Physics, Chemistry, and Pharmacy
University of Southern Denmark
Denmark
May 2022

Contents

1 Resumé

Brugen af bløde materialer til at konstruere selv-samlende strukturer og systemer har længe vist sig at være et formidabelt interessant felt. Og med nylige udviklinger inden for brugen af flydende krystaller, som er guidet af ustabiliteter og topoligiske defekter, har man kunne producere optiske fibre af god optisk kvalitet. Disse udgør et helt nyt grænseland for selv-samlende og rekonfigurerbar optik.

Hvis disse bliver realiseret, vil det være af stor betydning for nuværende teknologi, da det ville bane vejen for selv-reparerende og rekonfigurerbare optiske systemer.

Ved at gøre brug af surfaktantdrevne ustabiliteter i grænsefladen mellem smektiske flydende krystaller og en surfaktant opløsning, kan smektisk flydende krystalfibre realiseres. Men, de er sporadiske i deres produktion, de er ofte sammenflettede, og deres formation er i mindre grad tilfældig.

Her undersøger vi det samme eksperimentelle system og vi præsenterer en ny metode, hvorved enestående, lange, og lige fibre kan formes med en specifik orientation. Vi undersøger fiberformationen ved variende koncentration og grænsebetingelser, og viser også at disse fibre er afhængige af dynamikken i systemet.

Disse fibre kunne være vigtige i fremtidigt arbejde, da lange, lige, og rekonfigurerbare fibre er lette at arbejde med og utroligt brugbare.

2 Abstract

Employing soft matter systems to create self-assembled structures and systems has proven to be a remarkably interesting field. And with recent developments in utilising liquid crystal systems, guided by instabilities and topological defects, optical fibres of good optical quality have been produced. These constitute the frontier of a new generation of self-assembled and reconfigurable optics.

Self-assembled optics, if realised, will be of importance to science and industry alike, as they would pave the way towards self-repairing and reconfigurable optical systems.

By utilising surfactant driven instabilities in an interfacial region between a smectic liquid crystal and a surfactant solution, optical fibres of smectic liquid crystals were realised. However, these are sporadically formed, they are usually intertwined, and the production is not configurable.

In this work we investigate the same experimental system and we present a novel method of producing long, singular, and straight fibres with a specific orientation. We investigate the fibre formation by varying the surfactant concentration and the bounding surfaces, and show that the formation of

these fibres is highly dependent upon the dynamics of the system.
These singular fibres could be of use in future work, as straight and reconfigurable fibres are extremely useful.

3 Introduction

Liquid crystals (LCs) are a class of soft materials, that, although liquid in some temperature ranges, display certain characteristics of solid materials, such as their birefringent properties and ordered structure. They also have interesting properties under exposure to external fields. These properties make them extremely interesting for soft-matter scientists.
They have been used for decades in Liquid Crystal Displays (LCDs), but interest in them has recently been piqued due to their strong self-assembling properties, ability to form micro-structures with interesting light-guiding properties, [13], [18], and various other characteristics[8].
It has been shown[20], [22] that by addition of surfactants into a liquid crystal system, one can reduce the surface tension in the system in a manner that creates instabilities that can produce optical fibres, which are stabilised by the presence of a central topological line defect. These optical fibres have been shown[19] to have efficient light-guiding properties.
In this paper, I will investigate the formation of optical fibres in the smectic-A phase, and the light guiding properties of these fibres. I will focus on the interfacial region between a droplet of smectic liquid crystal and the surfactant which is injected into the system. This interfacial tube region displays various properties based on the concentration of surfactant, such as its growth rate and fibre-creation[20].
The effects of patterned substrates such as micro-ridges in various patterns, on the formation of the fibres will be investigated. The optical guidance properties of these fibres will then be investigated by utilising a specific dye, which orients itself with the liquid crystal. By then illuminating the region of fibres with a laser, one can demonstrate the optical properties of the fibres. [19]
I will firstly introduce theory, which is crucial in the understanding of liquid crystals, and how they are modelled and understood. A brief introduction to topology is then presented to better understand the system that is under investigation. The concepts of surface tension, interfaces, and surfactants are introduced. Then, a description of a simplified model of the optical guiding of the fibres is presented and a more complex model is briefly discussed. I then move on to the experimental part of the project.

4 Theory

In this section, I introduce all the various theories, which are needed to understand the system I am investigating.

4.1 Liquid Crystals

Liquid crystals are fluids, that have orientational order due to the geometry of the molecules they consist of. This paper will focus on the behaviour of rod-like molecule liquid crystals, and will therefore not discuss other types.
In liquid crystal theory one often refers to the vector denoted as the director, which is used to describe the system. It represents the direction in which the molecules are oriented. Another important characteristic of liquid crystals, is the phase they occupy.
In this work I will consider three phases, shown in figure 1:

1. **Isotropic phase**: The phase in which there is no preferred direction in the molecule's alignment, i.e., the director field has an isotropic distribution.

2. **Nematic phase**: There is a preferred direction, meaning the molecules align approximately with the local director field.

3. **Smectic Phase**: Aside from having orientational symmetry, such as the nematics, they also have a periodic layering of material normal to the director, which imposes additional constraints on the system.

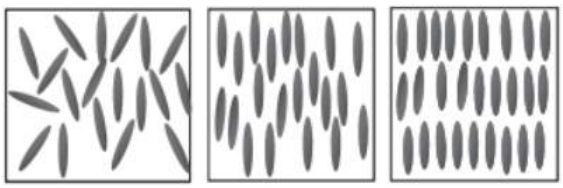

Figure 1: The three phases which are the main focus of this work. Left: Isotropic phase. Middle: Nematic phase. Right: Smectic A phase. Credits to Soft Matter Physics by Masao Doi [4].

4.2 The Order Parameter of the Nematic and Smectic A phases

In this section, I introduce the concept of employing an order parameter to describe a system. The order parameter is a measure of the order in that specific system. Order parameters will look differently, and have different constraints imposed upon them in different systems. I focus here on the nematic and smectic A order parameters.

4.2.1 The Nematic Order Parameter

To distinguish the isotropic and nematic phase, one can make use of a unit vector $\mathbf{u}$, which points in the direction of the molecule. By investigating [4] [3] the distribution function $\psi(\mathbf{u})$ of this unit vector, and the normalization condition that must be imposed upon it, and by utilising various arguments of extremum cases, and uniaxial symmetry assumptions, we can write:

$$S = \frac{1}{2}\Big\langle 3\cos^2(\theta) - 1 \Big\rangle \tag{4.1}$$

Where we have introduced the scalar order parameter, S, and θ, the angle between the director and the individual molecule, which is averaged over. In a perfect nematic phase, the average over the cosine term will result in 1, meaning the scalar order parameter for a perfectly nematic system is 1. However, if the distribution of θ is uniform, then $\langle\cos^2(\theta)\rangle = \frac{1}{3}$ and it gives us the perfect isotropic phase with S = 0. If liquid crystal molecules are aligned perfectly perpendicular to the director, S = $-\frac{1}{2}$[3]. The scalar order parameter is of great importance to the theory of modelling phase transitions in nematics, as the free energy density can be expressed in terms of S, and can be minimised in regards to it as well, as will be briefly discussed in section 4.3.4.

4.2.2 The Smectic A Order Parameter

The Smectic A order parameter consists of two different components [10]

1. A nematic component, with the amplitude s and phase $\mathbf{n}$
2. A component relating to the periodic density along the direction perpendicular to the layer, which is referred to as z.

$$\rho = \sum \rho_k e^{-i\boldsymbol{k}\cdot\boldsymbol{z}} \tag{4.2}$$

where $\mathbf{k} = m\frac{2\pi}{d_0}\mathbf{v}$, m is an integer, $\mathbf{v}$ is a unit vector along the normal to the layers. We define $q_0 = \frac{2\pi}{d_0}$ to be the corresponding elementary wave vector, where d_0 is the smectic layer spacing.
By considering a deformation described by the deformation field: $\mathbf{u} = u\mathbf{z}$, one can construct the smectic A order parameter:

$$\psi = \psi_0 e^{i\varphi} \tag{4.3}$$

Where the phase $\varphi = \mathbf{q}_0 \cdot \mathbf{u}$ is introduced to describe the modulation of matter density, and the reference smectic has $\varphi = 0$.

4.3 Energy and Curvature Considerations - Comparison of Nematic and Smectic

To properly model the various phases of liquid crystals, we have to take into account the various modes of deformation and the elastic energies associated with them. The modes of deformation will vary from different phases of the liquid crystal, due to various constraints imposed on the system, as will be explained below.

Generally, the energy considerations are in the form of elastic energy, phase energy, external field energy, and anchoring energy. These concepts will be introduced and briefly explained.

4.3.1 Nematic Elastic Energy - Frank-Oseen

Nematics have elasticity, since there is a preferred direction, i.e., the director, in the material. Following this, we can consider energy as a deformation of the nematic director $\frac{d\vec{n}}{d\vec{r}}$.

However, the nematic director has inversion symmetry, and rotations thusly have no energy penalty[4], [10], [3]. There are three main modes of deformation in such a system: the splay, the twist, and the bend. All of these correspond to a specific type of director deformation and can be seen below.

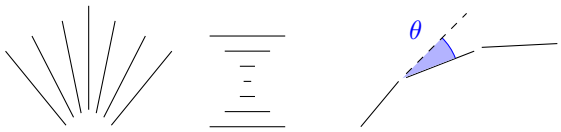

Where the left image is splay of the nematic director field, the middle image is twisting, and the right is bending.

The total energy of the system must then be:

$$E = E_{splay} + E_{twist} + E_{bend} \tag{4.4}$$

In energy considerations it is often convenient to rewrite things in terms of the elastic energy density [2], [10], [4], [3] called the Frank-Oseen energy:

$$F_{el} = \frac{1}{2}K_{11}\left(\boldsymbol{\nabla}\cdot\boldsymbol{n}\right)^2 + \frac{1}{2}K_{22}\left(\boldsymbol{n}\cdot\left(\boldsymbol{\nabla}\times\boldsymbol{n}\right)\right)^2 + \frac{1}{2}K_{33}\left(\boldsymbol{n}\times\left(\boldsymbol{\nabla}\times\boldsymbol{n}\right)\right)^2 \tag{4.5}$$

Where these constants of K_{11}, K_{22}, and K_{33} are the bulk elasticity constants for the various deformations. From unit calculations, it can be seen that the elastic constants has units of Newton [N], and their order of magnitude is approximately $10 \times 10^{-12}N$ (pico Newtons) for most liquid crystal systems[10].

K_{22} is often the numerically lowest constant, meaning the energy penalty of twisting is the lowest of the three.

However, to simplify matters, it is often assumed that all the three K-constants are the same, due to their order of magnitudes being so similar, in which case the energy density reduces to what is denoted as the reduced Frank elastic energy:

$$F_{el} = \frac{K}{2} (\boldsymbol{\nabla} \boldsymbol{n})^2 \tag{4.6}$$

4.3.2 Smectic A Elastic Energy

The elastic energy of a smectic A phase can be considered to have two contributions [10]: One from the nematic order parameter, which originates from the normal **n(r)** to the layers, and one from the 1D solid layers. The nematic bulk contribution is similar to the normal nematic elastic energy, but has no twist term[3], [10]:

$$F_{ne} = \frac{K_1}{2} (\boldsymbol{\nabla} \cdot \boldsymbol{n}) + \frac{K_3}{2} (\boldsymbol{n} \times (\boldsymbol{\nabla} \times \boldsymbol{n})) \tag{4.7}$$

$$F_{solid} = \frac{B}{2} \left(\frac{d - d_0}{d_0} \right)^2 = \frac{B}{2} \gamma^2 \tag{4.8}$$

Where d_0 is the equilibrium repeat distance between the layers, and d is the actual layer thickness, measured along **n**, and B is the Young modulus for the 1D solid.

To further investigate the various terms, consider a closed loop in a slightly deformed smectic. The number of traversed layers must equal zero in a closed loop, and can thusly be written as the following closed line integral, if the condition of no compression or dilation of the layers is met:

$$\frac{1}{d_0} \oint \boldsymbol{n} d\ell = 0 \tag{4.9}$$

By then invoking Stokes' theorem, we can thusly say:

$$\int \boldsymbol{\nabla} \times \boldsymbol{n} \cdot d\boldsymbol{S} = 0 \Rightarrow \boldsymbol{\nabla} \times \boldsymbol{n} = 0 \tag{4.10}$$

This results in the twist and bend energy equalling zero.

It has been shown that even with compression or dilation of the layers, the twist energy $\boldsymbol{n} \cdot \boldsymbol{\nabla} \times \boldsymbol{n}$ will remain zero. However, if the layers do not remain parallel, the bend energy contribution consists. One can investigate the relative strength of the two terms associated with this deformation, B and K_3. However, it is found [10] that B is much larger, and K_3 can then be neglected.

From these considerations, the free energy reduces to:

$$F = \frac{K_1}{2} \left(\boldsymbol{\nabla} \cdot \boldsymbol{n} \right)^2 + \frac{B}{2} \gamma^2 \tag{4.11}$$

4.3.3 Anchoring Energy

When considering how a liquid crystal will behave in a realistic system, one also needs to take into account what is called anchoring. Anchoring is a description of how the liquid crystal reacts to its surroundings or its boundary conditions. Two of the most basic types of anchoring are:

1. **Planar anchoring**: The liquid crystal molecules align parallel to the surface
2. **Homeotropic anchoring**: The liquid crystal molecules align perpendicular to the surface.

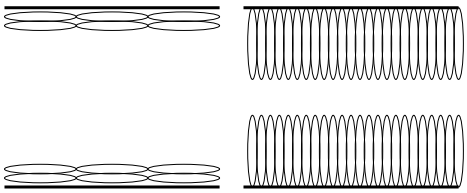

Figure 2: Left: Planar anchoring. Right: Homeotropic anchoring

These two anchorings can be induced in various ways, which is described in the methods section, 7, and are illustrated in figure 2. Anchoring energy can be written as the following:

$$W \cos^2 \left(\theta - \theta_0 \right) \tag{4.12}$$

This means that there is an energy penalty to shift from the anchored direction.

An important factor in experiments is the extrapolation length, which is given by:

$$\frac{K}{W} \propto length \tag{4.13}$$

Where $[W] = \frac{N}{m}$. The extrapolation length is a measure of how deeply the anchoring penetrates into the liquid crystal, before the bulk elasticity becomes the dominant force. The extrapolation length is on the order of micrometers, which defines the scale for most of the liquid crystal sciences.

4.3.4 Nematic and Smectic Phase Energy and Other Energy Contributions

To investigate the energy of the system near the phase transition, we can apply the general Landau theory [4], [10], [3]. Landau showed that for general systems, for which an order parameter describes the system, one can expand the energy near the phase transition via this order parameter. By utilising the nematic order parameter, the Landau-de Gennes theory can estimate the energy near the isotropic-nematic phase transition via the power series expansion of the order parameter. A similar procedure[10], Ginzburg-Landau theory, can be applied to the nematic-smectic phase transition, by

utilising the complex order parameter of smectics[1].

External fields can also contribute to energy considerations in liquid crystal systems, such as the Fréedericksz transition, which has been utilised immensely in liquid crystal systems such as the LCDs previously mentioned.

4.4 Topology and Defects

A topological defect is a particular point in space, where all anisotropic properties are lost. In the context of liquid crystals, it is a point where the molecules lose all preferential orientation, and revert to an isotropic phase.

Topological defects are often of interest in LC theory, due to the vector field quality of the nematic director of liquid crystals and the shapes it can occupy.

Generally, when a vector field is imposed upon a geometry, topology demands the formation of topological defects, in accordance with the geometry's Euler characteristic. The Poincaré-Hopf theorem states the relationship between defect charge and Euler characteristic:

$$\sum_{i}^{N} m_i = \chi(V) \tag{4.14}$$

Where $\chi(V)$ is the Euler characteristic of the geometry, N is the total number of singular points/defects, and m_i is the topological charge of the corresponding defect. The topological charge in this context is related to the amount of rotation in the vector field. However, as the energy of a defect has the relation

$$E \propto m^2 \tag{4.15}$$

half-integer charges are usually preferred over integer charges, depending on the dynamics of the system.

The additional constraint of energetic considerations and topological demands on a system is something that has been studied extensively [9], [1], and how it impacts the configurability and reconfigurability of the system.

In order to investigate the defects that are formed in the liquid crystals, we first look into the topology of such a system. Consider a director distribution such as shown in figure 3, left, where the nematic director field is mapped onto a sphere of identical dimensions to the system we are investigating. We will utilise this concept to look at various distributions in various dimensions.

[1] See appendix, equation 10.1 and equation 10.2

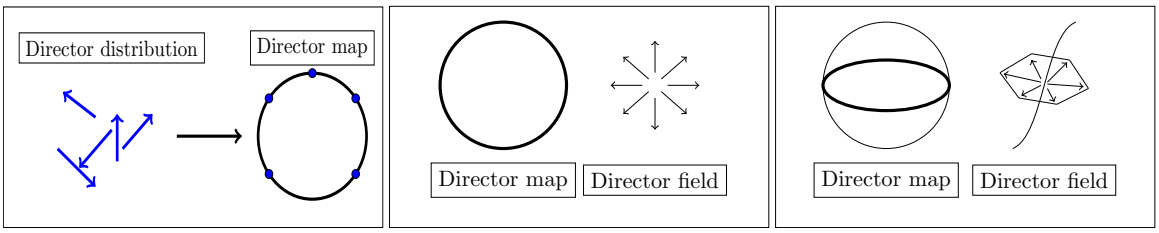

Figure 3: Left: A discrete director distribution is mapped onto a circle. Middle: A point defect in 2D of charge +1, and its continuous director distribution mapping. Right: A line defect in 3D, and its continuous director distribution mapping.

4.4.1 Point defect in 2D system

Consider a director field distribution, as shown in figure 3, middle. This distribution cannot be contracted into a single point in the mapping of the director field, meaning it is a proper topological defect, and due to the amount of rotation in the director field, it has topological charge +1.

4.4.2 Line defect in a 3D system - Nematic and Smectic

A line defect is a +1 charge 1D defect, which is extended into 2D, such as the one shown in figure 3, right.

It can be seen that this defect can be contracted into a single point on the map of the director field, meaning it is not a topological defect. From this it can be concluded that topological defects in 2D do not necessarily translate into topological defects in 3D; the defects can "escape" into the third dimension [3], see figure 4. This is the case for a nematic liquid crystal.

However, due to the imposed constraint of bending the director field not being allowed in the smectic A system due to the layer structure, these line defects cannot escape into the third dimension in smectic liquid crystals, and will thusly create actual, stable line defects. It is these line defects that I will study further in the experimental data.

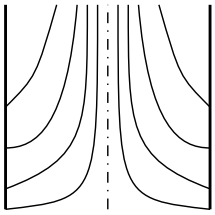

Figure 4: A visualisation of an escaped director field in 3D, with a central line defect.

4.5 Surface tension, Interfaces, and Surfactants

Surface tension, and specifically the rapid change in it, is something which is utilised to a great extent in the system we are investigating.

The molecular origin of surface tension is rooted in intermolecular forces[4]. In the bulk liquid intermolecular forces are averaged out by being approximately equal in all directions. At an interface between the bulk liquid and some other non-miscible liquid/gas, the intermolecular forces do not pull equally in all directions, but favour a pull towards the bulk, thus creating a restoring force

which drives molecules at the interface towards the bulk liquid.

Surfactants are molecules [4], which have a specific structure: A hydrophilic end and an oleophilic end. Due to this structure, they tend to adsorb to the interfaces between water-soluble materials and non-water-soluble materials. This effect lowers the surface tension of both materials, meaning interfacial regions where both materials are dissolved can be produced.

A vital measure of concentration, which varies for different surfactants, is the Critical Micelle Concentration (CMC), which is the concentration at which half of all surfactant molecules are aggregated in micelles. Micelles are spherical or ellipsoidally shaped aggregates of surfactant molecules. They arise due to contrasting properties of the ends of the surfactant, as one end would minimise its energy by being in contact with the solvent, and the other minimises its energy by shying away from the solvent. This arrangement can be satisfied by creating micelles, where, assuming the solvent is water, the hydrophilic head is on the outside of the micelle, and the oleophilic will be centred in the spherical structure, to be the closest to the other oleophilic ends.

Another important factor in surfactant theory is the Krafft temperature, which is described as the minimum temperature, above which micelles will form. Below the Krafft temperature the solubility will be beneath the CMC.

The interface seeking nature of surfactants can drive instabilities in the system they are affecting. As the surfactants adsorbs to the interface they drive instability in the region, due to the two immiscible fluids having less surface tension. Factors such as temperature, flow, or general dynamics in the system can drive the instability further, and if they are strong enough, the two immiscible fluids emulsify entirely.

4.6 Optical Guiding

Since we are interested in utilising the produced fibres as optical fibres, we must produce a theory that describes the light-guiding properties of the fibres to a satisfying degree.

The system we are investigating is one where there is an isotropic core, which corresponds to the topological defect, and a thick anisotropic layer, corresponding to the smectic layers.

If we simply consider the case where the optical fibre is considered to be a uniform core fibre, we can simplify things.

Starting with the Law of Refraction, also known as Snell's Law, from electrodynamics[6]:

$$\frac{\sin\theta_T}{\sin\theta_I} = \frac{n_1}{n_2} \tag{4.16}$$

If we now consider the case where the light moves from an optically dense material to one that is optically less dense, corresponding to the light inside the fibre, it follows: $n_1 > n_2$. The critical angle is given by:

$$\theta_c = \sin^{-1}\left(\frac{n_2}{n_1}\right) \tag{4.17}$$

If the incident angle is larger than the critical angle, $\theta_I > \theta_c$, then there is no refracted ray, only a reflected one. This is the concept of total internal reflection, by which optical fibres function.
A proper and formal treatment of the fibre's inner mechanics and electromagnetic field properties, would have to be derived from the Maxwell equations[17]. A short explanation is provided: One can utilise the cylindrical symmetry of the fibre and derive the Maxwell equations in cylindrical coordinates, from which separation of variables can be utilised. After a lengthy derivation, one arrives at the Bessel differential equation, which is an expression of the radial field function, and another differential equation for the angular field function. The solutions are expressed via the azimuthal mode number and the n'th order ordinary and modified Bessel functions. One can then take these solutions and apply them to various situations such as a uniform core fibre.

5 State-of-the-Art

Utilising liquid crystals as self-assembling materials has been studied for years, but recent developments in their self-assembling properties [15], have led to the investigation of their use in configurable and reconfigurable systems.
One such example [26] is the investigation of a system, in which nematic liquid crystal oligomer droplets are exposed to various environmental factors, and their reconfigurable properties are described.
Studies of highly-symmetric, reconfigurable grid-like structures have also been conducted [8], and found that by utilising optical manipulation, the structures can be configured to a desired pattern.
The defect structures of liquid crystals have also been of interest [23], [9], [11], [7], [1], [14] due to their ability to impose constraints and stability into a system, in which both nematic and smectic topological defects are shown to have light-guiding properties.
It has been shown that surfactant driven instabilities in a Smectic A liquid crystal interface results in the formation of optical fibres [20], and that the topological defects of the system act as a stabiliser of the fibres. These optical fibres have been shown to be uniform and of consistent diameter, and of good optical quality [19], which makes them prime candidates for optical applications.
Their optical properties have been investigated by utilising optical tweezers [19], [20] The production

of the fibres is sporadic and the proper methods of stabilisation are still under development.
Various methods of stabilisation have been attempted [22], [21] such as polymerisation of host media, polymerisation of the SmA liquid crystal, and cooling of the system.
Methods of trying to properly configure how the fibres are formed have also been studied [22], in which a novel method of utilising two different surfactant and temperature changes to induce a transition of nematic liquid crystal droplets into fibres is discussed.

6 Materials

6.1 Compounds

The liquid crystal compound used was 4-octyl-4'-cyanophenyl (8CB). At room temperature the compound 8CB is in the smectic A phase, and melts into the nematic phase at 33.0 ℃ and into the isotropic phase at 41.5 ℃[16]. It was purchased from Nematel Gmbh and used as is.
The surfactant used was hexadecyltrimethylammonium bromide $\leq$ 98% (CTAB) [24]. It was purchased from Sigma-ALDRICH and dissolved in its powder form.
A 0.5 % diluted solution of polyvinyl alcohol.
Dimethyloctadecyl[3-(trimethoxysilyl)propyl] ammonium chloride (DMOAP) which was purchased from Sigma-ALDRICH and used as is.
Cargille Immersion Oil Type 37
7-diethylamino-3,4-benzophenoxazine-2-one, Nile Red dye, purchased from Sigma-ALDRICH and used as is.

6.2 Hardware

Nikon ECLIPSE Ci POL 601295 Upright Manual Microscope.
Nikon Camera PS-Fi3.
The microscope was also fitted with a Quarter Wave plate, clear plate, and a tinted plate with the value $\lambda = 530nm$.
Nikon Achr 0.90 Polarizing condenser.
Lenses, all of the brand Nikon, of magnification 5X, 10X, 20X, and 50X were utilised.
Harrick Plasma Cleaner Expanded PDC-002 model, with accompanying PlasmaFlo gas mixer.
Laurell Technologies Spin Coater, Model WS-650Mz-23NPPB
Self-designed Heating element, with two Arcol HS50 10R F Wirewound resistors
Frederiksen Class 2 Modulated HE-NE Laser 0.5 - 1mW

6.3 Software

NIS - Elements AR 5.30.06 64-bit was used to view and capture images from the microscope.
ImageJ, with the plug-in Bio Format to properly handle the TIF files and their metadata, was used for image processing.
Julia 1.7.2 and appropriate libraries run through Visual Studio Code, was used for data processing and file handling.
Python 3.7 and appropriate packages run through the PyCharm IDE, was also used for data processing and file handling.

7 Methods

7.1 Cell Preparation and Glass Treatments

The cells consist of two main components: a bottom and top glass slide, with spacers in between. The bottom component has dimensions 2.5 × 2.5 cm. The top component has dimensions 2.5 × 1.9 cm.
These two components were cut using a handheld glass cutter into the appropriate sizes.
The cell components were then cleaned in a 50/50 mixture of 70% ethanol and distilled water. They were sprayed with ethanol and then blown clean using an airgun.
Depending on the experiment, one of three types of glass treatments were used.

1. **Untreated:** The untreated glass underwent no further treatment.

2. **Planar anchoring:** Planar anchoring was induced by utilising a spin-coater to deposit polyvinyl alcohol onto the surface, which was then rubbed with a piece of cloth in a specified direction to produce grooves in the polymer. These grooves create the conditions for planar anchoring, as the liquid crystal molecules will align in parallel with them.

3. **Homeotropic anchoring:** Homeotropic anchoring was achieved by submerging the glass into a solution of approximately 1% dimethyloctadecyl(3-trimethoxysilylpropyl)ammonium chloride, DMOAP, solution for approximately 15 minutes. The DMOAP acts as a silane coupling agent, thusly creating a chemical bond from which the alkyl chain sticks out of the surface. This "hairy" surface creates the conditions for homeotropic anchoring, as the liquid crystal molecules will align parallel with the alkyl chains.

They were kept in closed Petri-dishes until ready for use, so as to not be contaminated by particulate matter. If more than two weeks had passed, new homeotropic cells were produced.

7.2 Preparation of Surfactant Solutions

The CTAB solutions were prepared by employing the following unit analysis:

$$M_m \left[\frac{g}{mol}\right] \cdot c \left[\frac{mol}{L}\right] \cdot V[L] = M_{CTAB}[g] \tag{7.1}$$

Where M_m is the molecular weight of CTAB, c is the concentration which is desired, V is the volume of solution, and M_{CTAB} is the amount of CTAB required to make such a solution in grams. The amount of CTAB to make specified concentration was calculated, and weighed out on a microgram-scale. The CTAB is then thoroughly mixed with MilliPore water and heated, to ensure the purest solution possible.

7.3 Injection of Surfactant into Cells

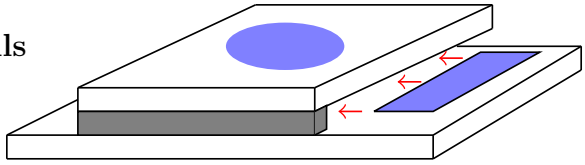

Figure 5: A sketch of the complete cell, with arrows indicating the capillary actions driving surfactant solution into the cell. The blue ellipsoid represent the liquid crystal droplet inside the cell. It is shown without clamps.

The liquid crystal, 8CB, is kept on a heating plate at approximately 45 degrees ℃, to ensure that it is in the isotropic phase, which allows the use of micropipettes in the handling of it, as it is too solid in the smectic A phase. A droplet of 8CB is put onto the bottom component of the cell, which is then fitted with an appropriate spacer on the edges. The cell is closed by putting the top component onto it; clamps are then used to ensure that the cell has the desired thickness. The cells are then injected with the surfactant solution by depositing the solution onto the lower edge of the bottom component and in contact with the edge of the top component, and allowing capillary action to carry it into the cell.

7.3.1 Retraction Method

A novel method has also been tried, which made use of a thin membrane of residual 8CB.
The cells are prepared as in the section above. However, instead of utilising clamps, they are secured by adding nail-lacquer between the spacers and the glass. After the top component has been placed, a weight equal to 995g is placed on top of the cell for 10 seconds. This temporary force resulted in the droplet spreading out further, which then retracts after the force is removed, creating a zone of retraction. See the left of figure 13 for reference.

7.4 Substrates

Micro-patterned substrates have been used in an attempt to physically guide the optical fibres. Two different compounds have been used, SU8 and PDMS.

7.4.1 SU8

SU8 is an epoxy-based negative photoresist, meaning it can be effectively cured onto surfaces via exposure to UV-light as exposure cross-links the material, whereas the SU8 that is not exposed to UV-light remains soluble and can be washed away.

7.4.2 PDMS

PDMS is a silicone-based organic polymer, and in this case, soft lithography has been used to imprint it onto a substrate in specified micro-patterned grooves.

7.5 Polarised Microscopy

Due to the orientational nature and ordering of liquid crystals, polarised microscopy is used to investigate the system. Polarised microscopy functions by sending light through a polariser, before it is transmitted through the sample. The transmitted light then goes through an analyser before hitting the lens and/or camera. The reason why this technique is used for liquid crystals resides in the birefringent properties of the liquid crystal[10]. A birefringent material produces two different waves, in accordance with their polarisation's angle with the LC optical axis. These two waves are coined as extraordinary and ordinary waves. Here we introduce the concept of the ordinary and extra-ordinary refractive indices, which is the refractive index experienced by the ordinary wave with a polarisation axis perpendicular to the optical axis of the crystal, and the refractive index experienced by the extra-ordinary wave with a polarisation axis parallel to the optical axis of the crystal, respectively.

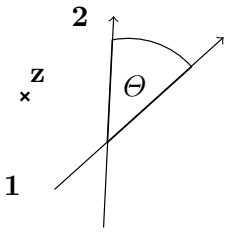

Figure 6: Angle of LC optical axis - polariser axis. z is the propagation direction.

When non-polarised light travels through a polariser, the intensity is given by[25]:

$$I = \frac{1}{2} I_0 \tag{7.2}$$

Malus' law states when incoming polarised light passes through a polariser, the outgoing intensity is given by:

$$I = I_0 \cos^2(\theta) \tag{7.3}$$

where I_0 is the initial intensity of the incoming light, and θ is the angle between the light initial polarisation angle, and the axis of the polariser.
When the light passes through an analyser and then a second polariser (called an analyser), the outgoing intensity is given by Malus' law, where θ is given by the angle between the axes of the polariser and analyser. However, as there is a birefringent lamina, the 8CB sample, in between the polariser and the analyser, the intensity is not quite that simple. We must take the birefringent properties of the material into consideration. Consider the case of figure 6, where **1** is the liquid crystal optical axis, and **2** is the incoming polarisation axis of mono-chromatic light.
By subdividing it into two cases, one of perpendicular polarisation and one of parallel polarisation, the intensity of the transmitted light will depend on the two scenarios:

$$I \rightarrow \begin{cases} A\sin(\Theta) \rightarrow n_0 \\ A\cos(\Theta) \rightarrow n_e \end{cases} \tag{7.4}$$

Where $A = \sqrt{I_0}$, n_0 is the ordinary refractive index, and n_e is the extra-ordinary refractive index.
The perpendicularly and parallel polarised light will travel through the material at different speeds, which is expressed via the respective refractive index:

$$v_0 = \frac{n_0}{c} \cdot d \qquad , \qquad v_e = \frac{n_e}{c} \cdot d \tag{7.5}$$

Where c is the speed of light and d is the thickness of the birefringent material.

When the waves have travelled through the medium, they will have a phase difference, due to the varying speeds, which is given by:

$$\Delta\phi = \frac{2\pi d}{\lambda_0}\left(n_e - n_0\right) \tag{7.6}$$

Where λ_0 is the wave length of the incident light.
We can then gather all of this to calculate the total transmitted intensity of light[10], [4]:

$$I = A^2 \sin^2(2\Theta) \sin^2\left(\frac{\pi d}{\lambda_0}\Delta n\right) \tag{7.7}$$

Where this specific formula assumes that the LC optical axis is perpendicular to the vertical axis.
Where it is then evident, that the intensity is a squared sinusoidal signal, varying with the angle

between polariser axis and liquid crystal optical axis. The second term is dependent upon system constants, such as the incident wavelength, sample thickness, and difference in ordinary and extra-ordinary refractive index. It is this term that leads the behaviour described in a Michel-Levy[2] chart, which is the selection of specific wavelengths to be transmitted based on the thickness of the sample. The intensity signal peaks at $\Theta = \frac{\pi}{4}$, and is zero for angles 0 and $\frac{\pi}{2}$. By utilising the birefringent properties of the liquid crystal and polarised microscopy, we can thusly construct an image where there are only bright spots where there is an angle between the propagation direction and the LC optical axis.

7.6 Wave-guiding in the fibres

The liquid crystal is doped with >1 wt% Nile Red dye, which is a dye that aligns with the LC molecules. The dye allows the light-guiding properties to be detected more efficiently.
A semi-transparent mirror is at a tilt angle of approximately 45°, with regards to the horizontal, underneath the condenser of the microscope, which enables the lensing of the Helium-Neon laser through the polariser, sample, and then analyser and through into the camera/lens of the microscope.

7.7 Data-processing

Various scripts and programs written by myself have been used throughout the process of analysing the resulting data. In this section, I will briefly describe the underlying processes and maths. I will not go into detail about the various programming languages or specifics regarding how the code is implemented[3].

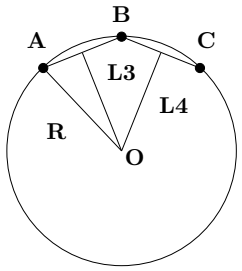

Figure 7: The three points on the circumference, where A = (x_1, y_1), B = (x_2, y_2), C = (x_3, y_3). L3 is the perpendicular bisector of AB, and L4 is the perpendicular bisector of BC. R is the radius. O is origo.

7.7.1 Normalisation of Data

There were several factors which contributed to the need for normalisation of the resultant data, and the method in which it was implemented. The micro-pipettes that were available were not precise enough to produce the needed size of liquid crystal droplet, meaning the droplets ranged in volume of about 0.15 μL - 0.4 μL. However, even if precise micro-pipettes had been available, a much more

[2]See appendix, figure 21
[3]See appendix, listing 1 and listing 2

extensive set-up is needed to produce 0.1μL droplets. As
mentioned in section 7.3, the 8CB is kept at approximately 45 ℃, to ensure that it is in the isotropic phase. Even with the procedure of heating up the pipette-tip, the 8CB cools and reverts back into the smectic phase quickly, meaning that 0.1 μL of material is incredibly hard to handle.
Due to this uncertainty in volume of the initial droplet, the raw data cannot be assumed to be dependent according to the same parameters and factors. Thus, I decided to normalise the data via the initial radius of the droplet.
The radius of the droplet while in the cell, is difficult to measure, and I decided to instead measure it by utilising an algorithm, and cross-reference with a caliper.
The algorithm's input is three points, $A = (x_1, y_2),\ B = (x_2, y_2),\ C = (x_3, y_3)$, on the circumference of the circle. It finds the lines in between points A and B, and points B and C. By then analysing the perpendicular bisector of these two lines, and finding their intersection one can find the centre of the circle, or origo. It then calculates the distance between point A and the origo, which is the radius. See figure 7. The data was normalised by simply dividing it by this initial radius.

7.7.2 Angular Probability Density Distribution

In this section I describe the method of finding the relation between micro-grooves in the cell, and the orientation of the produced fibres. The images were loaded into ImageJ and every intersection of a fibre and a micro-groove was noted and drawn onto the picture.

By utilising the ROI manager in ImageJ, one can find the angle of a drawn line. This angle is a reference angle, in regards to a horizontal reference line. However, depending on which way the line is drawn, you are either given a negative angle, ψ, or positive angle, Θ, with respect to the horizontal. See figure 8. This was taken into account when writing the algorithm. If the negative angle ψ is given, we simply utilise $\Theta = 180 - |\psi|$, to find the positive angle Θ. The following then holds:

$$\zeta = \Theta - \Phi \tag{7.8}$$

By utilising this method, we can produce a distribution of the smallest angle between the fibre and micro-groove, which ranges from 0°-90°. The program also normalises it, to produce the probability

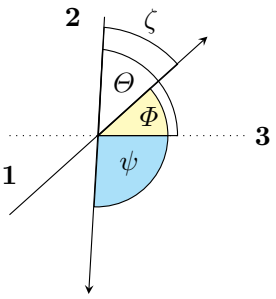

Figure 8: Example of the angular set-up, between fibre and micro-groove, where 1 is the fibre, 2 is the micro-groove, and 3 is the reference zero-point for the angles.

density function (PDF). I utilised Sturge's Rule, which states, if the number of bins in the histogram is denoted as η:

$$\eta = \lceil \log_2(n) + 1 \rceil \tag{7.9}$$

Where n is the sample size, and $\lceil\rceil$ denotes the ceiling function.

8 Results and discussion

8.1 Interfacial region and Fibre growth

The first solutions of CTAB I produced had concentrations: 8.8mM, 20mM, 40mM, and 65mM, see [20] for reason behind these concentrations. Experiments were conducted with cells of thickness $\sim 50\mu$m, and these concentrations produced an interfacial region but no fibres.
The interfacial region also seemed to be proportional to the concentration, which was an unexpected result as this seemed to contradict previous findings. Another surprising result was the time-scale on which these regions were forming. It was expected that the region would be forming within a time-scale of 3 minutes[20], but as can be seen on figure 9, left, the time-scale is substantially larger, as the last measurements were performed at 45 minutes.

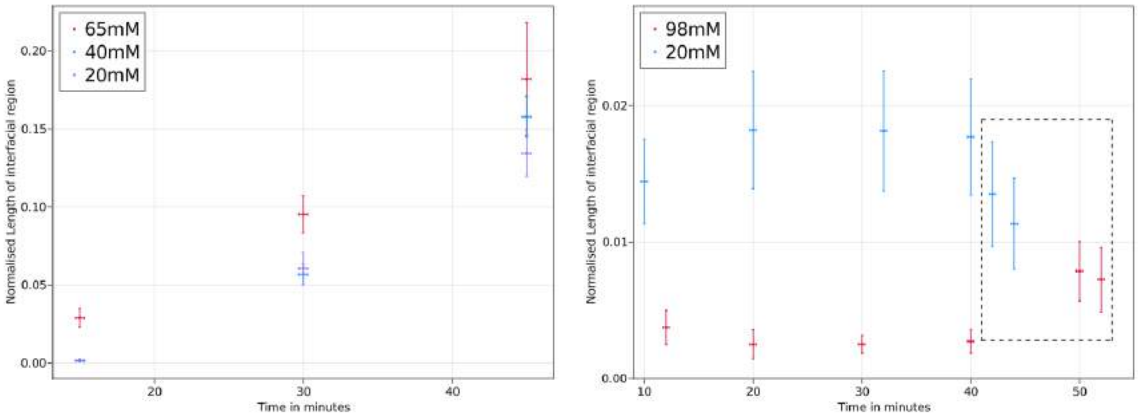

Figure 9: Left: Interfacial region growth as a function of time, and concentration. Right: Burst behaviour at late stages of development in 98mM and 20mM concentration of CTAB. The error bars along the x-axis represents 20 seconds, as that was how long it took to take the pictures that are averaged over. The error bars along the y-axis are the standard error of the mean.

To probe into the reason behind the larger time-scales, we turn to the properties of the CTAB

molecule.

Firstly, the critical micelle concentration (CMC) is found[5] to be approximately 0.9mM, meaning our concentrations all are above the CMC.

Secondly, we turn to investigate the diffusion of the CTAB molecule, to see whether the adsorption to the interfacial surface is too slow for processes to happen. The diffusion coefficient[12] of CTAB is found to be somewhat constant, $\sim 6 \times 10^{-10} \frac{m^2}{s}$, in the regime of 0.1mM - 0.4 mM, and it is slightly higher in the regime of 0.01mM - 0.1mM where it is $\sim 7 \times 10^{-10} \frac{m^2}{s}$.

Consider a disk of area πr^2 where r is half the length of the CTAB molecule, $\sim 3nm$. We consider how long it takes this disk to diffuse its own area:

$$\frac{\pi \left(1.5 \times 10^{-9} m\right)^2}{6 \times 10^{-10} \frac{m^2}{s}} \approx 1.17 \times 10^{-8} s \tag{8.1}$$

Meaning the adsorption replenishing rate to the interfacial region is on the order of magnitude of tens of nano-seconds.

To validate the set-up of the experiment, I investigate the system's dependence on the Krafft temperature of CTAB. The Krafft temperature of CTAB is ≈ 20℃[20], and to ensure that the experiments are conducted above this temperature, a heating pad for the cells is constructed.

By utilising this heating pad, experiments of systems with 20mM and 305mM solutions were conducted at $\approx 25 - 26$ ℃.

No interfacial region formed in the relatively short time-periods which were observed in the system of 20mM.

In the experiment of 305mM it was found that it responded in similar time-scales, as the non-heated experiments[4].

To further verify the system set-up, I tested the thickness of the sample spacers, by pressing them in between glass slides, and employing the microscope the probe the thicknesses[5]. I then conducted experiments with varying thicknesses, and found that the thickness played no significant role in the time-scales involved.

All following experiments were conducted with a cell of thickness $\sim 50\mu m$.

Since no fibres were being created in the original sample concentrations, I produced solutions with a much higher concentration, ranging from 65mM - 305mM.

After testing these, I found that the same larger time-scales were relevant, but after approximately

[4]See appendix, figure 22
[5]See appendix, figure 23

40-50 minutes, a sudden burst of growth in the length of the interfacial region appeared in most samples. Figure 9 right shows the irregular behaviour produced by the burst of growth, which is encased in a dashed region for high-lighting. The 20mM had a somewhat regular growth, until minute 40 where the burst behaviour started. The system of 98mM did not seem to have a regular growth, but also showcases the burst behaviour, as can be seen in both the data and on the pictures. Figure 10 and 11 showcases the burst behaviour of the system.

Since region growth seemed proportional to the concentration of CTAB, this seemed to suggest that the concentration was becoming increasingly higher as time went on. Evidently, since I was working on larger time-scales than expected, and the concentration was increasing with time, evaporation had become an issue for truthful data collection. In addition, the evaporation of surfactant solution also produced additional dynamics in the system's staticity, as air bubbles formed and interrupted the system, in such a way that the interfacial region was disturbed and data could no longer be meaningfully collected.

To fix the issue of evaporation, a heavy oil was added to the edges of the lower component of the cell after injection of surfactant to seal the cell.

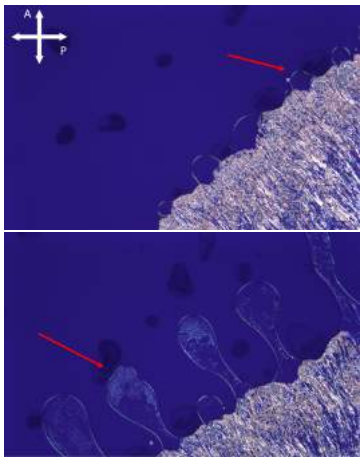

Figure 10: Burst behaviour of 98mM system. Top: Minute 50. Bottom: Minute 56. Polariser and analyser axis is indicated in the picture. The same polariser and analyser axis is used in all following pictures

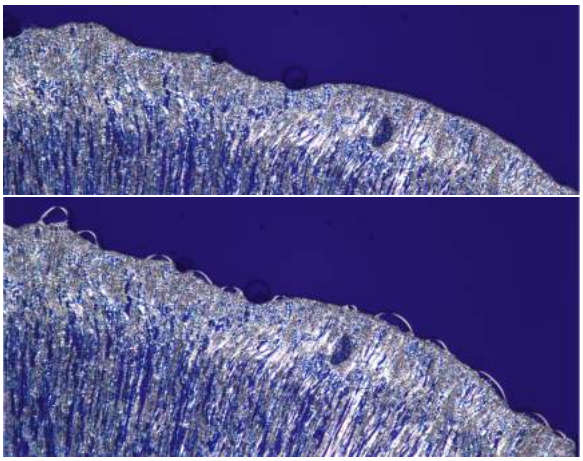

Figure 11: Burst behaviour of 20mM system. Top: No interfacial region, in this part of the droplet at minute 38.
Bottom: Suddenly an interfacial region occurs at approximately minute 40.

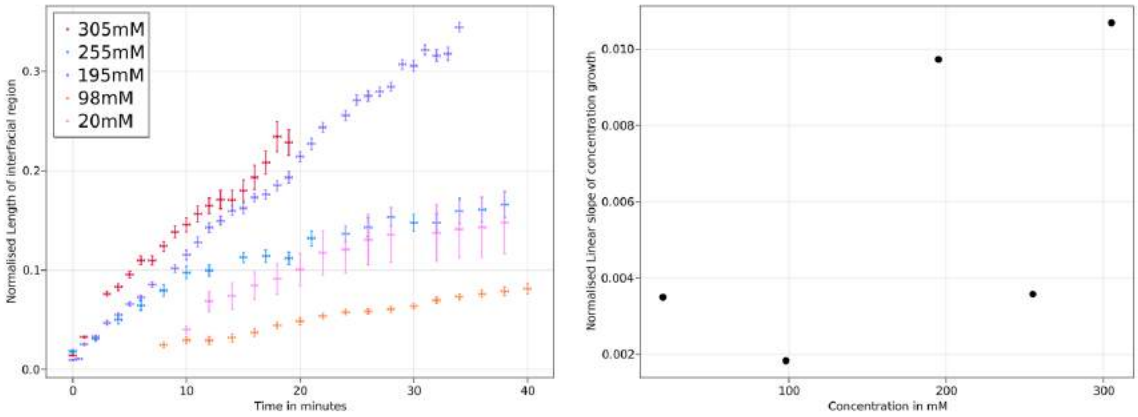

Figure 12: Left: The interfacial region's growth evolution of various concentrations as a function of time. The error in the x-direction is approximately 20 seconds, as that was the time it took to take the pictures that are averaged over. The error in the y-direction is the standard error of the mean. Right: A linear fit is found by utilising a first-order polynomial, of which the slope is plotted as a function of concentration.

The graphs seen in figure 12 are the results of the addition of oil to the edges of the cells. No burst behaviour was observed in these, but evaporation was evident as the samples were observed again after ∼72 hours, and most of the surfactant solution had evaporated. However, it did not seem to affect the experiments as it had been slowed sufficiently.

8.1.1 Retraction Method

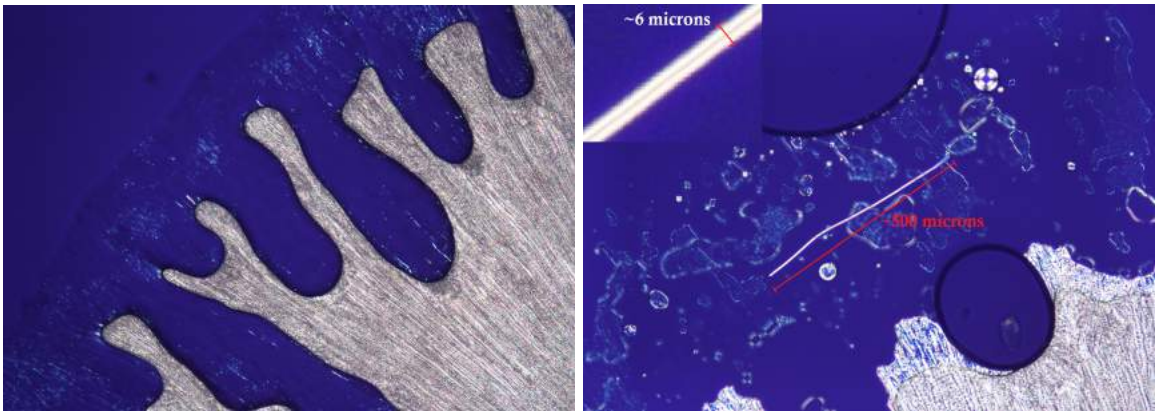

Figure 13: Right: The thin membrane of residual 8CB in the retraction region. The tendril-like structure of the bulk 8CB is due to the temporary pressure, and varies from sample to sample. With less pressure, the retraction region presented itself as an annulus of varying thickness. Left: A fibre formed away from the bulk material, in the retraction region. The azimuthally formed fibre, seemed to have formed with flow as the injection site was above it. The insert shows the 2D cross-section of the concentric ring structure of the fibre.

By utilising the retraction method, I found that the fibres being created in the thin membrane left over in the retraction region, had a strong dependence on fluid dynamics.
They were often formed away from the bulk material, as there was no bulk material in the region. Generally, they were smaller in diameter and not as long as the fibres formed from bulk creation. There were formed much quicker than their bulk-counterparts, but also seemed less stable as they dispersed after 3-5 minutes. However, they were generally also much straighter than fibres formed from bulk. I managed to produce singular, long, straight, and thick fibres utilising this method. See figure 13, right and figure 14. I suggest the reason for these azimuthally formed fibres, was their dependence on the flow in the system, and as they were not formed from bulk, they could simply flow along the current.

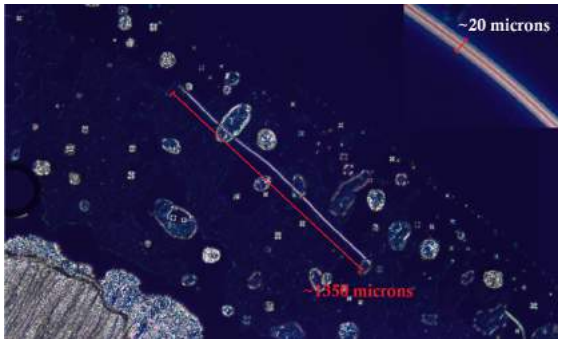

Figure 14: A longer, azimuthally formed optical fibre, created using the retraction method. The fibre has a consistent diameter of approximately 20 microns, and a length of approximately 1350 microns.

8.2 Substrates and Micro-patterned grooves

I performed several experiments employing the micro-patterned grooves in the bottom component of the cell and found very little evidence that supported physical guiding of the fibres.
In the first experiment, which utilised the 195mM system, air-domes centred around the concentric ring structure of the micro-grooves impeded flow of surfactant and generally hindered proper data collection. See figure 15
To remedy this, the substrate and PDMS grooves were plasma-cleaned, to provide a more hydrophilic surface, to encourage flow of surfactant.
This resulted in a much higher spread of the 8CB, due to it being immiscible with water, but this did not seem to affect the formation of fibres.

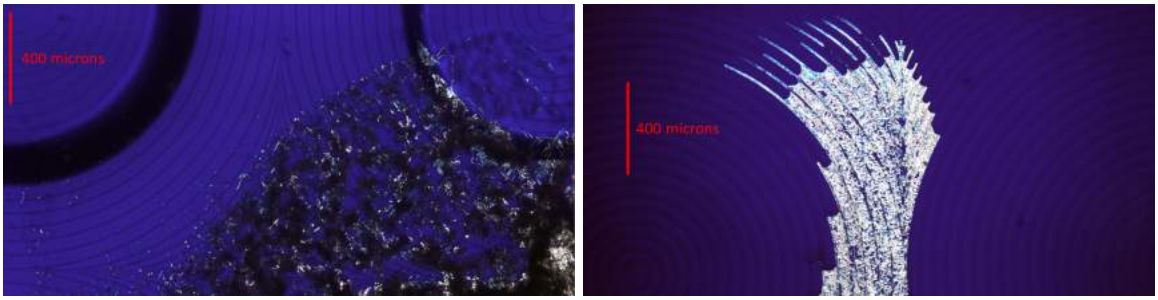

Figure 15: Right: Air-domes which hindered flow of surfactant solution. Left: Plasma-cleaned surface, which resulted in higher spread of the 8CB, due to the hydrophilic surface.

I found that for the concentric ring structure of the grooves, the orientation of the fibres produced the probability density functions as shown in figure 16:

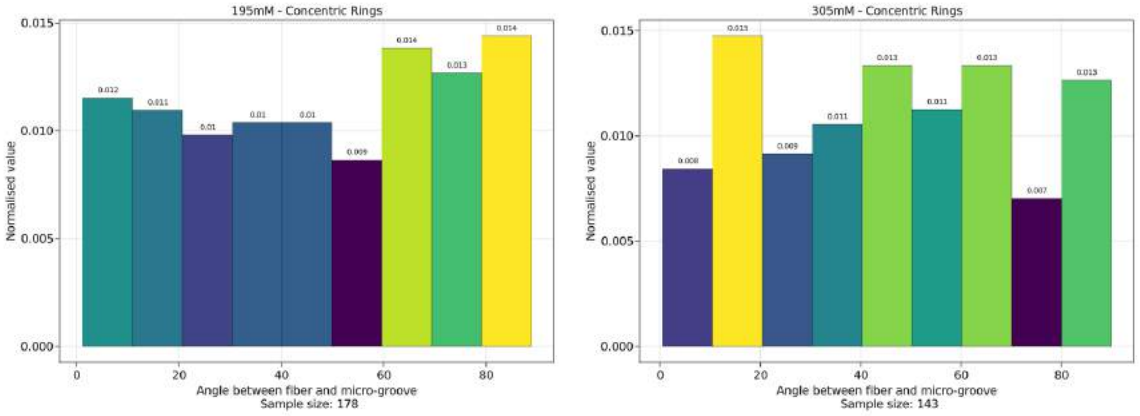

Figure 16: Left: Probability Density Function for 195mM system with concentric ring micro-groove structure. Right: Probability Density Function for 305mM system with concentric ring micro-groove structure, where the grooves had been plasma-cleaned before the experiment, to encourage solution flow.

If the system is free of influence from physical guiding or flow-orientation, these PDFs should originate from a uniform distribution.

This is tested by utilising a non-parametric Kolmogorov-Smirnov test, where the null-hypothesis is that the data originates from a uniform distribution, and a two-sided p-value is given. It is tested with a 95% confidence interval. By utilising the Kolmogorov-Smirnov tests, it is evident that while the distribution is not necessarily from a uniform distribution, which could very well be due to the small sample size, the null-hypothesis cannot be disregarded entirely.

Concentration:	195mM	305mM
H_0 verdict	Fail to reject	Fail to reject
Two-sided p-value	0.3333	0.8597

In addition, I conducted experiments with linear, parallel micro-grooves. The first experiment was set up in such a way, that the micro-grooves' orientation was parallel to the injection site, and thusly parallel to the flow of surfactant. By utilising the method described in section 7.7.2, the probability density function on the left of 17 is produced:

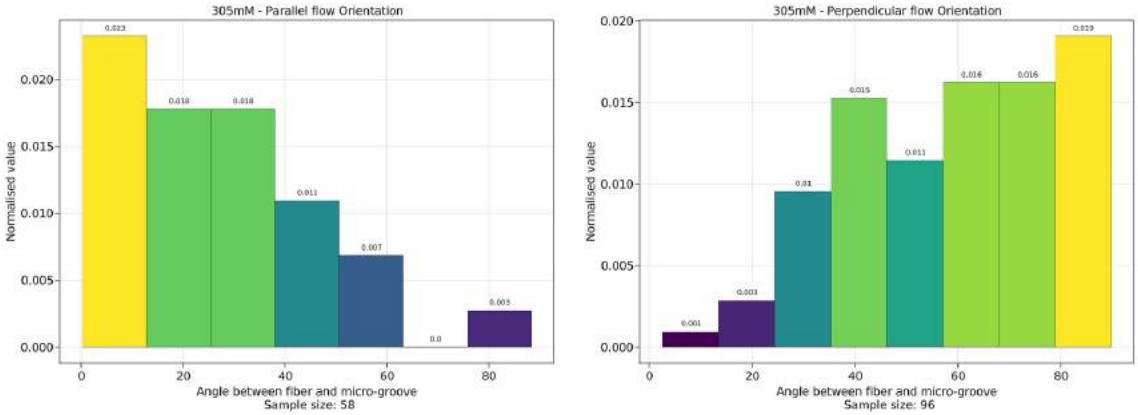

Figure 17: Probability Density Function for various flow/groove alignments. Left: Flow orientation is parallel with groove orientation. Right: Flow orientation is perpendicular on groove alignment.

A clear trend can be seen on the left of figure 17, which is that the fibres tend to align to the grooves, as there is a sharp peak at 0 °- $\sim$ 15°and then the probability falls off towards perpendicularity.

Due to the relatively small sample size, which arises from the limited production of fibres, the PDF will have irregularities, such as is seen at approximately 65 °- 75 °. To investigate whether this trend of alignment is a factor of the environment, or if the fibres are physically guided by the grooves, another experiment was conducted, where the grooves were instead oriented perpendicular to the flow of surfactant, which produces the PDF as shown on the right of figure 17:

Flow - Groove orientation	Parallel	Perpendicular
H_0 verdict	Rejected	Rejected
Two-sided p-value	$> 10^{-6}$	$> 10^{-6}$

Again, there is a clear trend, however, the inverse trend of the parallel alignment. The fibres are much more likely to orient themselves perpendicularly to the grooves. These are also tested using the Kolmogorov-Smirnov test, and it is evident that they are not from a uniform distribution.

Slight photographic evidence of physical guiding is included in figure 18. However, even with these accounted for in the data-analysis, they bear no statistical significance to the overall results.

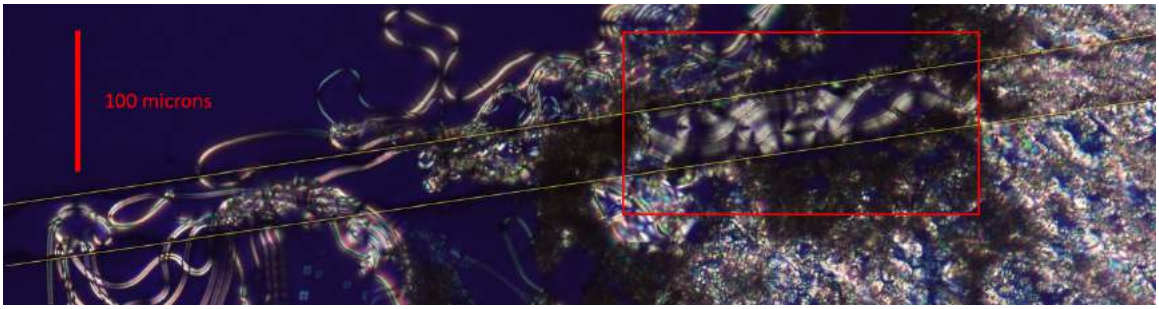

Figure 18: Physical Guiding of optical fibres in 305mM system, with perpendicularly aligned micro-grooved in comparison to flow orientation. The yellow lines indicate the boundaries of the micro-grooves.

8.3 Planar and Homeotropic Anchoring

The planar and homeotropic anchoring functioned as intended, as can be seen on figure 19.

The planar anchoring presents itself as a fully bright region, indicating that the anchoring is successful, due to reasons explained in section 7.5.

The homeotropic anchoring presents itself as a bright interface region, but the bulk liquid crystal remains dark, as the liquid crystal optical axis remains perpendicular to the polarisation axis of the incoming polarised light. The induced interfacial region does not appear in the same fashion in the two anchorings, and the planar anchoring seems to have a more well-defined region, whereas the homeotropic seems riddled with instabilities and lacks well defined boundaries.

In addition, the homeotropic system does not seem to produce bulk fibres, but only the smaller and thinner retraction fibres.

These results suggest that planar anchoring is the optimal anchoring, when trying to probe the system we are inter-

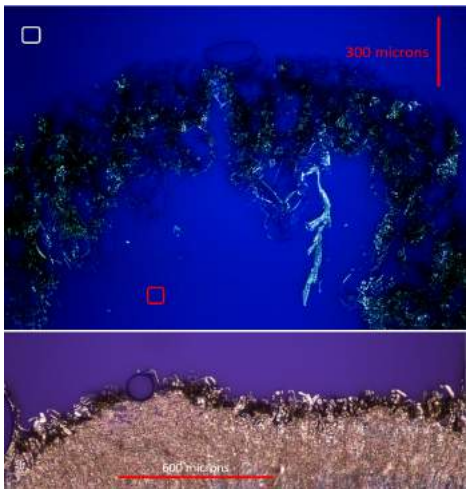

Figure 19: Top: Homeotropic anchoring. Inside and outside the droplet is labelled with a red and white square, respectively. It can be seen that the inside of the droplet has no transmitted light. Bottom: Planar anchoring, which shows consistent transmitted light inside the droplet.

ested in. Most of the experiments were conducted with untreated glass, which regularly produces random planar anchoring, indicating that it was the correct set-up.

8.4 Wave-guiding properties

The wave-guiding properties of the fibres were probed by utilising the method described in section 7.6, and the results can be seen below.

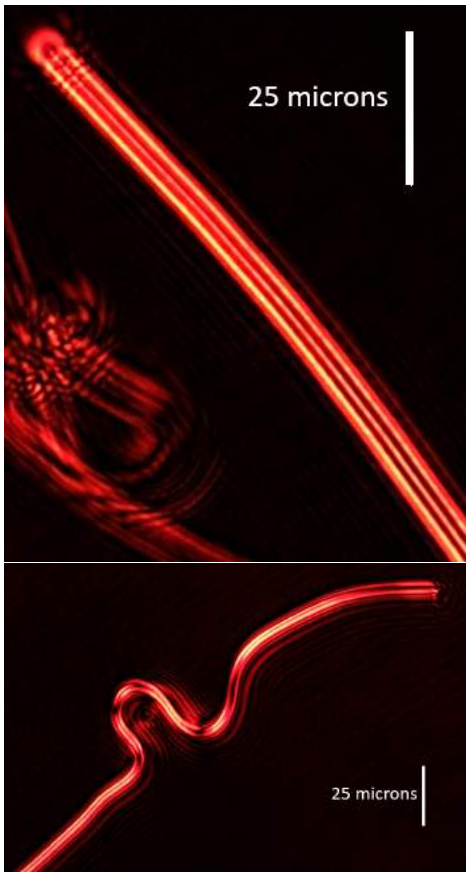

Figure 20: Wave-guiding in optical fibres, doped with fluorescent Nile Red dye, illuminated by a red laser.

The wave-guiding of the fibres seems to be comparable with the established theory, of the various modes travelling along the edge of the fibre. A possible explanation for the bright centres, could be lensing due to the Nile Red dye.

9 Conclusion

I have conducted experiments, where I have attempted to document the relation between the surfactant concentration and the growth of the interfacial region between a liquid crystal droplet and the surfactant solution inside a closed cell.

These interfacial regions also produce optical fibres. An attempt to physically guide the production and orientation of these fibres has been made, by utilising micro-patterned substrates. The light-guiding properties of said produced fibres have been investigated. A novel method to produce singular, straight fibres has also been tested.

With the data provided by this work, no proper relation between concentration of the instability driving surfactant and the growth of the interfacial region can be established. The reason for the deviation from already established work cannot be determined. From conducted experiments, no statistically significant physical guiding from patterned micro-grooves in the creation of fibres can be concluded. However, in the process, a dependence on the flow of surfactant was revealed. The light-guiding properties of the optical fibres have been shown, and they seem

to be comparable to the theory. A well-received result is the consistent formation of azimuthally produced fibres, due to the predictability in their formation orientation and general singularity. This predictability and configurability of their formation is a step-forward in the utilisation of these fibres.

References

[1] M. Čančula, S. Žumer, and M. Ravnik. Generation of vector beams with liquid crystal disclination lines. *APS - Physical Review E*, 2014.

[2] P. Collings and M. Hird. *Introduction to Liquid Crystals: Chemistry and Physics*. Liquid Crystals Book Series. CRC Press, 1997.

[3] P. G. de Gennes and J. Prost. *The Physics of Liquid Crystals*. Clarendon Press, 2nd edition, 1998.

[4] M. Doi. *Soft Matter Physics*. Oxford University Press, 2013.

[5] J. M. Goronja, L. A. M. J., D. B. M., M. A. M., S. D. R., and P. N. D. Determination of critical micelle concentration of cetyltrimethyl-ammonium bromide: Different procedures for analysis of experimental data. *Hem. Ind.*, 2015.

[6] D. J. Griffith. *Introduction to Electrodynamics*. Pearson, 4th edition, 2013.

[7] I. Gryn. *Self-assembly of Structural Defects and Nano-objects in Liquid Crystal Films*. Phd thesis, Universita' Della Calabria, 2015.

[8] V. S. R. Jampani, Y. Sasaki, K. Le, F. Araoka, and H. Orihara. Reconfigurable topological defect arrays in nematic liquid crystals. *SPIE*, 2017.

[9] F. C. Keber, L. Etienne, S. Tim, D. S. J., G. Luca, B. M. J., M. M. Christina, D. Z., and B. A. R. Topology and dynamics of active nematic vesicles. *Science*, 2014.

[10] M. Kleman and O. Lavrentovich. *Soft Matter Physics: An Introduction*. Partially Ordered Systems. Springer-Verlag New York, New York, 2004.

[11] T. Machon, H. Aharoni, Y. Hu, and K. D. Randall. Aspects of defect topology in smectic liquid crystals. *Commun. Math. Phys.*, 2019.

[12] T. Movchan, I. V. Soboleva, E. V. Plotnikova, and A. K. Shchekin. Dynamic light scattering study of cetyltrimethylammonium bromide aqueous solutions. *Colloid Journal*, 2012.

[13] I. Muěvič. Integrated and topological liquid crystal photonics. *Liquid Crystals*, 41, 2013.

[14] I. Muševič, M. Čančula, M. Ravnik, and S. Žumer. Liquid microlenses and waveguiding from bulk nematic birefringent profiles. *Optics Express*, 24, 2016.

[15] I. Muševič, H. Peng, M. Nikkhou, and M. Humar. Self-assembled liquid-crystal microlasers, microresonators, and microfibres. *SPIE*, 2014.

[16] A. R. K. Nassrah, I. Jánossy, V. Kenderesi, and T. Tóth-Katona. Polymer–Nematic Liquid Crystal Interface: On the Role of the Liquid Crystalline Molecular Structure and the Phase Sequence in Photoalignment. *Polymers*, 13, 2021.

[17] T. Okoshi. *Optical Fibers*. Academic Press, 1982.

[18] K. R. Peddireddy. *Liquid Crystals in Aqueous Ionic Surfactant Solutions: Interfacial Instabilities and Optical Applications*. Phd thesis, University of Göttingen, 2014.

[19] K. R. Peddireddy, V. S. R. Jampani, S. Thutupalli, S. Herminghaus, C. Bahr, and I. Muševič. Lasing and waveguiding in smectic A liquid crystal optical fibers. *Optics Express*, 21, 2013.

[20] K. R. Peddireddy, P. Kumar, S. Thutupalli, S. Herminghaus, and C. Bahr. Myelin structures formed by thermotropic smectic liquid crystals. *APS March Meeting Abstracts*, 2014, 2014.

[21] K. R. Peddireddy, I. Muševič, V. S. R. Jampani, S. Čopar, C. Bahr, M. Mur, and K. V. Le. Self-shaping liquid crystals droplets by balancing bulk elasticity and interfacial tension. *PNAS*, 118, 2021.

[22] K. R. Peddireddy, I. Muševič, V. S. R. Jampani, S. Čopar, C. Bahr, M. Mur, and K. V. Le. Self-shaping of liquid crystals into superstructures for photonic applications. In *SPIE*, 2021.

[23] R. Preusse, E. George, S. Aghvami, T. Otchy, and M. A. Gharbi. Hierarchical Assembly of Smectic Liquid Crystal Defects at Undulated Surfaces. In *Soft Matter*, 2020.

[24] M. J. Rosen and J. T. Kunjuppa. *Surfactants and Interfacial Phenomena*. John Wiley and Sons, 4th edition, 2012.

[25] J. Walker, D. Halliday, and R. Resnick. *Principles of Physics*. Wiley, 10th edition, 2014.

[26] W.-S. Wei, Y. Xia, S. Ettinger, S. Yang, and A. G. Yodh. Molecular Heterogeneity drives reconfigurable nematic liquid crystal drops. *Nature*, 2019.

10 Appendix

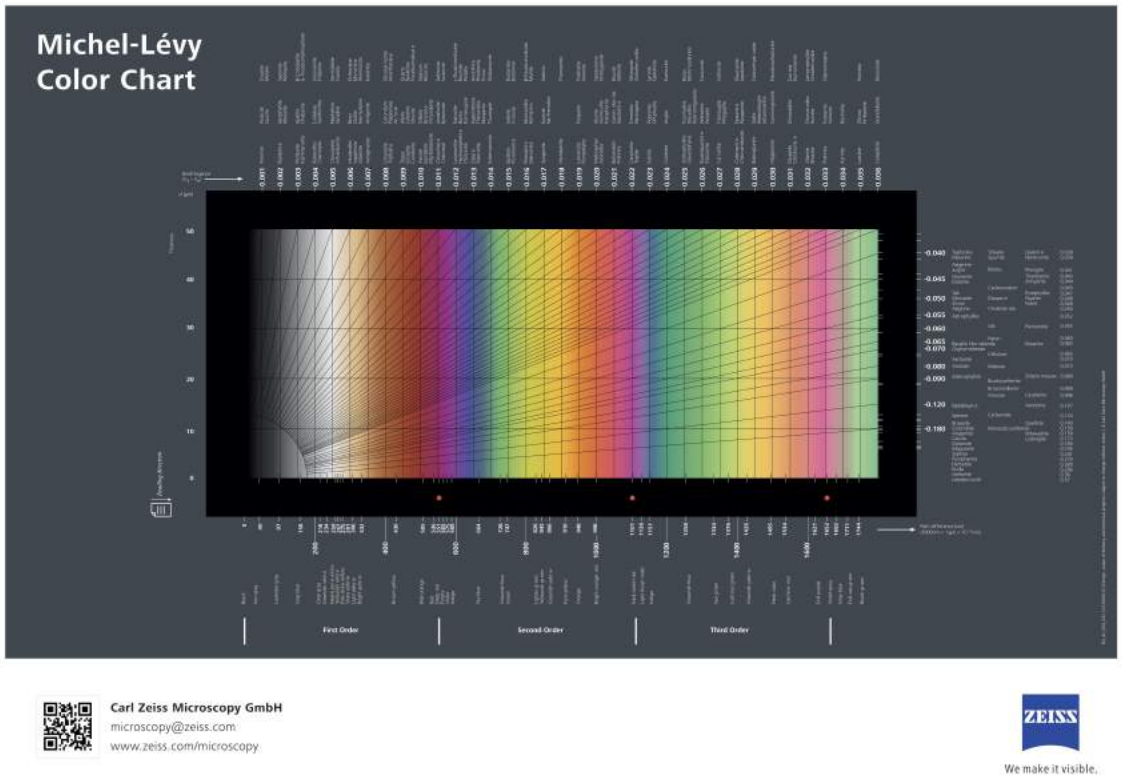

Figure 21: A Michel-Lévy chart, which visualises the connection between the birefringence of a material, the observed colour of that material, and the thickness of the material sample. Provided by: By ZEISS Microscopy from Germany - Michel-Lévy interference colour chart, CC BY-SA 2.0, `https://commons.wikimedia.org/w/index.php?curid=45625127`

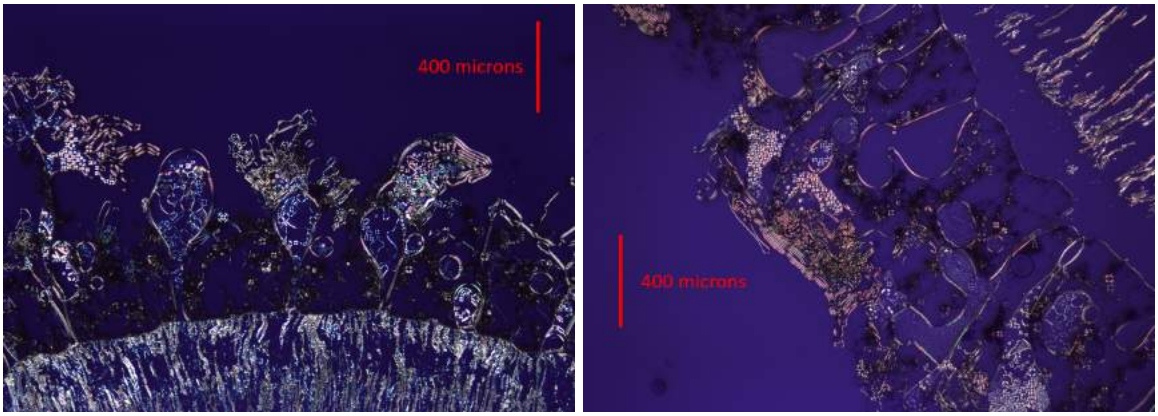

Figure 22: Left: System of 305mM, that has not been heated while performing the experiment. Right: System of 305mM that has been heated to a temperature of 26℃ while performing the experiment. Both pictures were taken at minute 14. By visual inspection, it is clear that the response is operating on similar time-scales.

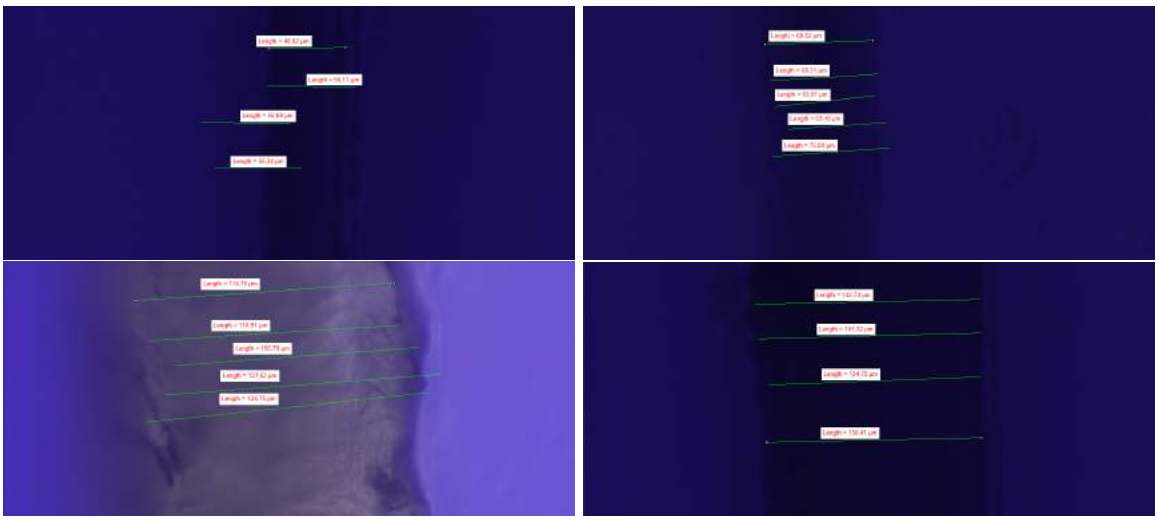

Figure 23: Thicknesses of various spacers. Top left: Aluminium foil, which was the most used. Top right: Semi-hard plastic. Bottom left: Parafilm, which was only used once, as it is too malleable, and deform easily. Bottom right: Scotch tape. The measurements might seem to not add correctly to the picture, however, the overlay is a product of several pictures, so they are factual.

The Ginzburg-Landau phase energy expression, for the nematic-smectic phase transition:

$$F_{SmA} = \alpha|\psi|^2 + \frac{\beta}{2}|\psi|^4 + \frac{1}{2M_{\parallel}}\left|\frac{\partial\psi}{\partial z}\right|^2 + \frac{1}{2M_{\perp}}\left|\left(\nabla_{\perp} - iq_0\delta\boldsymbol{n}\right)\psi\right|^2 \tag{10.1}$$

The Landau-De Gennes phase energy expression for the isotropic-nematic phase transition:

$$F_{ph}(S;T) = \frac{1}{2}A\left(T - T_c\right)S^2 - \frac{1}{3}BS^3 + \frac{1}{4}CS^4 \tag{10.2}$$

Listing 1: Finding Radius Function

```
function find_radius() # It takes in three points with x, y coordinates
  path_to_zipped = raw"C:\Users\olive\Desktop\Zipped"
  file = open_dialog("Chose a file", GtkNullContainer(), String["*.csv"])
  data = Tables.matrix(DataFrame(CSV.File(file)))
  x1 = data[4] # Due to the formatting, start at index 4
  x2 = data[5]
  x3 = data[6]
  y1 = data[7]
  y2 = data[8]
  y3 = data[9]
  temp = x2^2 + y2^2 # Calculating the various lengths/bisectors
  bc = (x1^2 + y1^2 - temp) / 2
  cd = (temp - x3^2 - y3^2) / 2
  det = (x1 - x2) * (y2 - y3) - (x2 - x3) * (y1 - y2)
  if (abs(det) < 1.0e-10) #Checking if the points are colinear
    return None
  end
  # Center of circle
  cx = (bc*(y2 - y3) - cd*(y1 - y2)) / det
  cy = ((x1 - x2) * cd - (x2 - x3) * bc) / det
  radius = [((cx - x1)^2 + (cy - y1)^2)^(.5)]
  full_file = string(path_to_zipped, "\\", split(file, raw"\\")[7][1:end-4]
    , "Zipped", ".csv")
  CSV.write(full_file, DataFrame([radius], [:radius]))
  return radius
```

```
26 end
```

Listing 2: Angle distribution calculation

```
1  function angles_distribution()
2    file = open_dialog("Chose a file", GtkNullContainer(), String["
     *.csv"])
3    vector_of_data = Tables.matrix(DataFrame(CSV.File(file, select
     =[2])))
4    title_of_plot = string(split(file, raw"\\")[7][1:5], " -
     Concentric Rings")
5    angles = Float64[]
6    ranges = 1:2:length(vector_of_data) - 1
7    for i in eachindex(vector_of_data)
8      if vector_of_data[i] < 0
9        vector_of_data[i] = 180 - abs(vector_of_data[i]);
10     end
11   end
12   for i in ranges
13     if vector_of_data[i] > vector_of_data[i + 1]
14       theta = vector_of_data[i]
15       phi = vector_of_data[i + 1]
16     else
17       theta = vector_of_data[i + 1]
18       phi = vector_of_data[i]
19     end
20     angle = abs(theta - phi)
21     if angle > 90
22       angle = 180 - angle
23     end
24     push!(angles, angle)
25   end
26   sample_size = length(angles)
27   number_of_bins = Int64(ceil(log2(sample_size) + 1))
```

```
28      xlabel_fig = string("Angle between fiber and micro-groove \n
    Sample size: ", sample_size)
29      fig_hist = Figure()
30      axhist = Axis(fig_hist[1,1], xlabel = xlabel_fig, ylabel = "
    Normalised value", title = title_of_plot)
31      hist!(axhist, angles, bins = number_of_bins, normalization = :
    pdf, bar_labels = :values, color = :values,
32      strokewidth = 0.5, stroke_color = (:black, 0.5), label_size =
    10)
33      title_of_saved_figure = string(raw"C:\Users\olive\Desktop\Uni\
    Bachelor\6. Semester\Bachelor\\", title_of_plot, ".png")
34      Makie.save(title_of_saved_figure, fig_hist)
35      display(fig_hist)
36      uniform_fit = StatsPlots.fit(Uniform, angles)
37      StatsPlots.qqplot(angles, uniform_fit)
38      ExactOneSampleKSTest(angles, uniform_fit)
39  end
```